Harnessing geographic information system and street view imagery for thermal gradient distribution auditing

Lang Zheng[a], Weisheng Lu[*], Jianxiang Huang[b], Fan Xue[a]

[a] Department of Real Estate and Construction, Knowles Building, The University of Hong Kong, Pokfulam, Hong Kong SAR, China

[*]Corresponding author, KB503, 5/f, Department of Real Estate and Construction, Knowles Building, The University of Hong Kong, Pokfulam, Hong Kong SAR, China, wilsonlu@hku.hk

[b] Department of Urban Planning and Design, Knowles Building, The University of Hong Kong, Pokfulam, Hong Kong SAR, China

Abstract

Assessing and managing the thermal environment within urban streetscapes is of paramount importance for the health, livability, and ecological sustainability of metropolitan regions. However, due to a scarcity of high-precision historical street thermal environment data for prediction and modeling, existing urban thermal environment classification assessment studies suffer from low resolution (> 30m) or limited research scope (e.g., community-level), resulting in less accurate and comprehensive insights. This study introduces an innovative framework for constructing large-scale urban street-level thermal gradients using classified samples derived from the spatial structural features of street points. The core of this framework lies in the k-means unsupervised classification algorithm. This approach integrates detailed local geographic information system (GIS) data with street view features, calculated through semantic segmentation of Google Street-View-Panorama using the DeepLabV3 model. This allows for the categorization of a vast array of high-precision street points based on spatial structural similarity, a key factor influencing the similarity of street thermal environment features. By selecting appropriate samples for on-site thermal environment measurements within each category and subsequently extrapolating this knowledge to the thermal environment classification of each category, this framework facilitates the rapid creation of high-precision street-level thermal gradient models across extensive urban areas.

Keywords: Street view panoramas; Geographic information system, Semantic segmentation; K-means; Thermal gradient

1. Introduction

Urban spatial structure is an abstract or generalized description of phenomena within geographical spaces, encompassing aspects such as the distribution of elements, their proportions, and relative positions [1]. These spatial geometric concepts play a crucial role in understanding and interpreting the mechanisms underlying urban environments, transportation, and socio-economic developments [2, 3]. However, with the acceleration of urbanization and

the expansion of urban scale, the complexity of the urban spatial structure is constantly growing, making the collection, analysis, and interpretation of urban data increasingly challenging [4].

In the past few decades, the incorporation of geographic information systems (GIS) into urban spatial analysis has significantly advanced research endeavors. GIS facilitates the visualization, analysis, and interpretation of urban space by integrating various types of data [5]. For instance, remote sensing data obtained via satellites and airborne sensors are presented in the form of regular pixel arrays (i.e., raster), with each pixel representing a specific geographical area and containing attribute information about that region, can be utilized for monitoring environmental changes, urban development, land use, and so on [6, 7]. Numerous research methodologies have emerged around these data, including place syntax and spacematrix [8, 9]. By extracting shape, size, and location data of urban elements (e.g., street greenery, street networks, transportation nodes, and public facilities), indices such as building density, public space ratio, and mixed-use distribution are calculated, revealing detailed urban characteristics encompassing sustainability, livability, and vibrancy [10]. Although GIS possesses notable advantages and value in addressing large-scale urban research issues, limitations in data perspective and format may impact its ability to discern nuances in urban environments. Specifically, the top-down viewpoint and raster data format imply a limited level of detail in the geographic space, potentially leading to inaccuracies and errors when analyzing urban spatial structures and morphology [11].

With the proliferation of mobile devices, the widespread application of wireless communication technology, and the development of services such as Google Street View, street view data volume has been increasing continuously [12]. Meanwhile, virtual audits have gradually emerged, progressively replacing traditional on-site inspections. By leveraging advanced data analysis technologies, such as machine learning and computer vision, it is possible to automatically extract from street view imagery (SVI) datasets detailed urban spatial structure features unattainable from satellite images and other frequently used data sources [13]. Furthermore, SVI offers a visual experience that originates from the human perspective, which plays a pivotal role in evaluating research questions involving psychological perception such as the urban thermal environment [14].

Although significant progress has been made in recent years in urban spatial analysis using SVI, there remain two main limitations that urgently need to be addressed. Firstly, in extracting street view features from SVI, numerous studies primarily focus on the most intuitive perceptual experiences in urban spaces, such as the sky view factor (SVF), tree view factor (TVF), and building view factor (BVF), while neglecting the potential effects generated by other diverse urban characteristics (e.g., urban functions, building materials) and surrounding geographical conditions. In cities with complex functional zoning and geographical environments, such as Hong Kong, these features may vary significantly from street to street. Such an approach is incapable of holistically assessing the genuine characteristics of urban spaces, potentially resulting in biases in the actual analysis. Secondly, current SVI research typically concentrates on urban features that are easily quantifiable or have complete historical data, such as a city's GDP, population growth, traffic flow, and household poverty levels. However, for more complex or subjective urban features, such as the distribution of thermal gradient in cities, the lack of street-level high-resolution historical thermal data and unified evaluation criteria makes the extraction of urban spatial thermal environmental characteristics based on SVI challenging.

This study aims to develop a comprehensive urban street thermal gradient classification framework that integrates GIS and street feature data calculated from DeepLabV3 semantic segmentation model, complementing the strengths of both to provide a high-precision solution

for urban thermal environment classification. These data are used as inputs to the k-means unsupervised classification model. Appropriate samples are selected from each classified category, and their on-site thermal environment data are collected to establish the thermal gradient for each category of street space. This framework addresses the difficulty and inaccuracy of urban street thermal gradient classification where the labeled data is unavailable or scarce. In addition, the study conducts a detailed statistical analysis of the individual data for each category, aiming to provide comprehensive and detailed guidance and reference information for different populations in seeking, planning, and constructing cool spaces in urban environments.

The remainder of this paper is organized as follows: Section 2 offers a concise review of prior research on urban spatial feature auditing, with emphasis on urban thermal environment. Section 3 elaborates each sub-stage within the proposed methodology. Section 4 outlines the datasets used for experimentation, and Section 5 reports the research results and findings. Section 6 discusses the implications and limitations of the study, while Section 7 presents the conclusion, summarizing the main insights.

2. Related works

2.1 GIS-based urban thermal pattern modeling

GIS-based urban thermal pattern mapping encompasses two primary research streams. Thermal infrared (TIR) remote sensing techniques are employed to directly retrieve land surface temperature (LST) [15]. LST plays a pivotal role in regulating the temperature of the lower layer urban atmosphere, as it determines the radiation and energy exchange at surface level, the internal climate of buildings, and the comfort level of urban dwellers [16]. Consequently, comparative analyses of the relationships between LST and other urban features can further reveal intricacies and diversity within the urban thermal environment [17]. Roth, et al. [18] pioneered exploration of the potential of TIR technology for detecting land surface radiant temperature in three coastal cities and explored its relationship with land use. The field has since garnered widespread attention and continuous refinement and improvement in related method (e.g., emissivity correction). Lo, et al. [19] matched LST with the complexity of urban environment factors such as land use and land cover (LULC) and normalized difference vegetation index (NDVI) to spatially model the urban heat island effect. Weng, et al. [20] discussed the relationship between LST and vegetation abundance in the urban heat island context. In addition to LULC and NDVI, Huanchun, et al. [21] investigated the correlations between LST and several other factors, including modified normalized water index, point of interest density, green space and plot ratio, as well as building and road density.

Unlike the direct acquisition of LST, prediction-based methods build on conclusions of data correlation derived from previous studies, indirectly estimating urban thermal patterns through related GIS data. This typically involves establishing models such as regression models, machine learning models, and so on. For example, Iino and Hoyano [22] utilized weather parameters (e.g., air temperature, relative humidity, solar radiation, wind velocity) along with GIS data (e.g., base map of urban planning, traffic information, vegetation map) to numerically simulate surface temperature distributions through a heat balance algorithm. Equere, et al. [23] integrated terrain factors and other morphological parameters to develop an artificial neural network (ANN) model to predict LST. In addition, some studies predict future changes in urban thermal patterns based on historical data. Maduako, et al. [24] did so based on 28 years of LST data, with a 7-year interval. Kafy, et al. [25] integrated LST, LULC, normalized difference built-up index, and normalized difference bare soil index data from 1999, 2009, and 2019 as inputs for an ANN model to predict the urban thermal field variance index for 2029 and 2039.

2.2 SVI for urban thermal feature auditing

While LST has been used as the most common assessment metric for modelling urban thermal pattern in the recent literature, the limited ability of top-view raster GIS data to capture details of urban spatial features makes it potentially unrepresentative of the level of warming at the street level [26]. Therefore, recent studies have extensively employed computer vision techniques to retrieve three-dimensional object information from two-dimensional SVI and establish a comprehensive understanding of this imagery. Thermal environment modeling is an important research branch in this field, with numerous studies utilizing various street view features, among which SVF is one of the most critical as it directly affects the canyon's radiant temperature and indirectly impacts its air temperature [27]. For example, Bourbia and Boucheriba [28] and Johansson [29] sketched urban heat islands and thermal comfort based on SVF and height to width (H/W) ratios derived from fisheye images. Carrasco-Hernandez, et al. [30] used fisheye images constructed from GSV to calculate SVF and estimated short-wave global irradiance using the Rayman model. Richards and Edwards [31] analyzed the proportion of green canopy cover using GSV and estimated the shading effect of trees on the annual radiation reaching the ground.

However, only a limited number of studies have considered the impact of both GIS and street view features on urban thermal patterns. For instance, Andrew, et al. [32] employed road, terrain, vegetation, and building attributes along with SVF to model road surface temperatures. Wei, et al. [33] integrated LULC, SVF, TVF, and BVF features and predicted LST using multiple linear regression and various machine learning models. All of these publications have, to varying extents, neglected certain GIS and street view features, and are limited in terms of the study area size and time available for data collection. This reveals existing research gaps while simultaneously offering insightful references for the evaluation of street thermal gradient.

3. Research methodology

The overall structure of the proposed framework is presented in Fig. 1. The coordinates of Google Street-View-Panorama (GSVP) acquisition points are first determined using urban road network data. GSVPs are generated by synthesizing street view perspectives from four directions at each coordinate point (phase 1: data collection and processing). Subsequently, for each coordinate point, the GIS data (i.e., LULC, elevation, and slope) are extracted from remote sensing data and digital elevation model using ArcMap software. The GSVPs are fed into a well-trained semantic segmentation model, the output of which is employed for extracting SVF, TVF, and BVF (phase 2: feature extraction and calculation). The collected GIS and street view feature data for each coordinate point will serve as input for an unsupervised classification model to facilitate data classification and subsequent analysis (phase 3: clustering analysis). The on-site measurement data of samples from each category will set the thermal levels of the respective categories (phase 4). The details of each sub-step are introduced as follows.

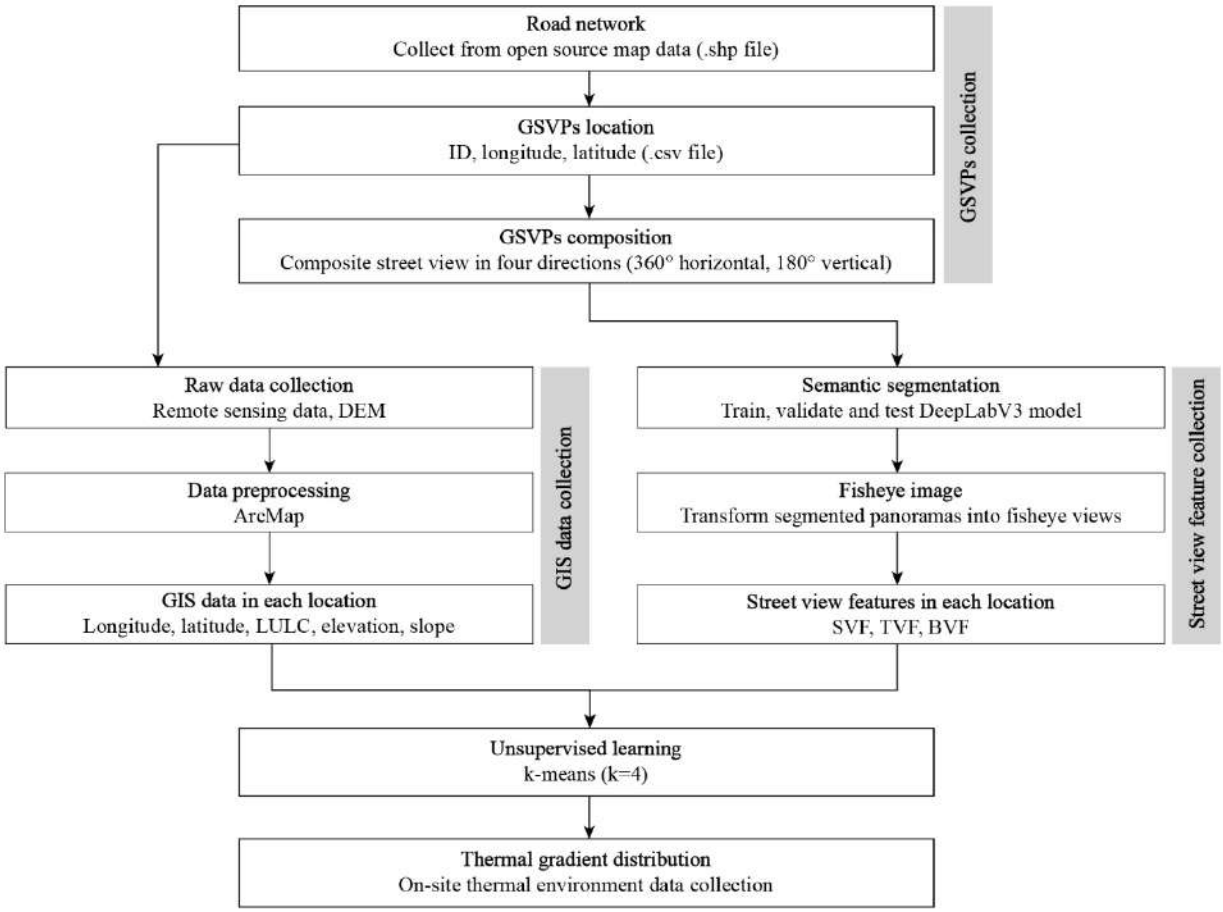

Fig. 1 The proposed framework for street thermal gradient classification

3.1 Data collection and processing

The vector data of the road network in the study area is obtained from OpenStreetMap, an open-source global geographic information repository featuring a data structure using basic elements such as nodes, ways, and relations. Subsequently, the downloaded road data is imported into the ArcMap software for data filtering and editing. Roads where people are less likely to remain for extended periods according to attributes such as steps, tunnels, bridges and those under construction are excluded. Data collection points are generated every 50 meters along the remaining roads, assigned a unique ID, and their geographical coordinates (longitude and latitude) are recorded. This information serves as the basis for obtaining panoramic images from the GSV service.

In order to achieve bulk acquisition and management of GSVPs, the unique IDs of each previously acquired data collection point are traversed, and based on their corresponding geographical coordinates, street view images at four angles (0°, 90°, 180°, 270°) are fetched from the GSV service. These images are then stitched together to form a panoramic image. In this step, distortion correction, image alignment, and smoothing of transition areas is applied to the street view images, which are projected onto the spherical coordinate system to eliminate distortions caused by perspective projection. Next, the overlapping areas between adjacent images are automatically detected and matched to achieve precise image alignment. To further improve the stitching effect, transition areas are smoothed at different scales, ensuring that the final generated GSVPs possess high quality and reliability.

3.2 Feature extraction and calculation

3.2.1 GIS feature extraction

LULC data within the GIS parameters is derived from remote sensing data, specifically from *Landsat 8/9 OLI/TIRS C2 L1* (operational land imager/thermal infrared sensor collection 2 level 1) [34]. L1 remote sensing data encompasses the fundamental tier of spectral information. Through the data collected by multispectral and hyperspectral sensors, the spectral reflectance characteristics of various surface materials and ecosystems (i.e., LULC) across different bands can be captured, identified, and differentiated. To improve the sensitivity and accuracy of the data, several common metadata filters are employed, with cloud cover percentage, for instance, restricted between 0% and 10%.

The obtained multi-band raster datasets are imported into ArcMap software and processed by creating a composite band file. Subsequently, a supervised classification approach is employed for the LULC analysis. This procedure encompasses two critical steps. The first is training sample generation. To ensure accuracy of the classification results, a minimum of 10 training samples are created for each LULC type. The creation of these samples is based on the training sample manager function within the ArcMap image classification tools. Each LULC type is assigned a unique name (e.g., urban, bare surface, vegetation, water) and corresponding value (e.g., 1, 2, 3, 4) for identification during the subsequent classification process. The second step is conducting supervised classification using the interactive supervised classification function for classification. Input parameters include the composite band file and the training sample management file. Ultimately, a classified raster dataset comprising four land-use types is generated.

Elevation data within the GIS parameters is directly obtained from the digital elevation model, which originates from the advanced spaceborne thermal emission and reflection radiometer (ASTER) global digital elevation model (DEM) dataset [35]. Based on the acquired elevation data, slope information for the study area is extracted using the slope function in the ArcMap spatial analyst tools. This process involves calculating spatial derivatives on the DEM data to obtain slope values for each grid cell.

Upon acquiring the three GIS parameters for the study area, corresponding values are extracted using the ArcMap extract multi values to points tool according to the collection point coordinates in section *3.1*. Ultimately, these GIS values, along with geographical coordinates, are stored in a CSV file, facilitating their retrieval during the subsequent creation of an unsupervised classification task dataset.

3.2.2 Street view feature calculation

Street view features are derived from semantically segmented GSVPs, which are obtained from the DeepLabV3 model [36]. At the core of the DeepLabV3's architecture lies ResNet50 [37], a 50-layer deep residual network that incorporates residual modules to alleviate the vanishing gradient issue, thereby facilitating the network's ability to delve deeper into learning image features (Fig. 2). Within ResNet50, residual modules serve as the fundamental building blocks, permeating the entire network structure. Each residual block consists of multiple convolutional layers, and by incorporating an identity mapping following the convolutional operation, the input feature map is combined with the convolutional result through element-wise addition, subsequently generating the output feature map.

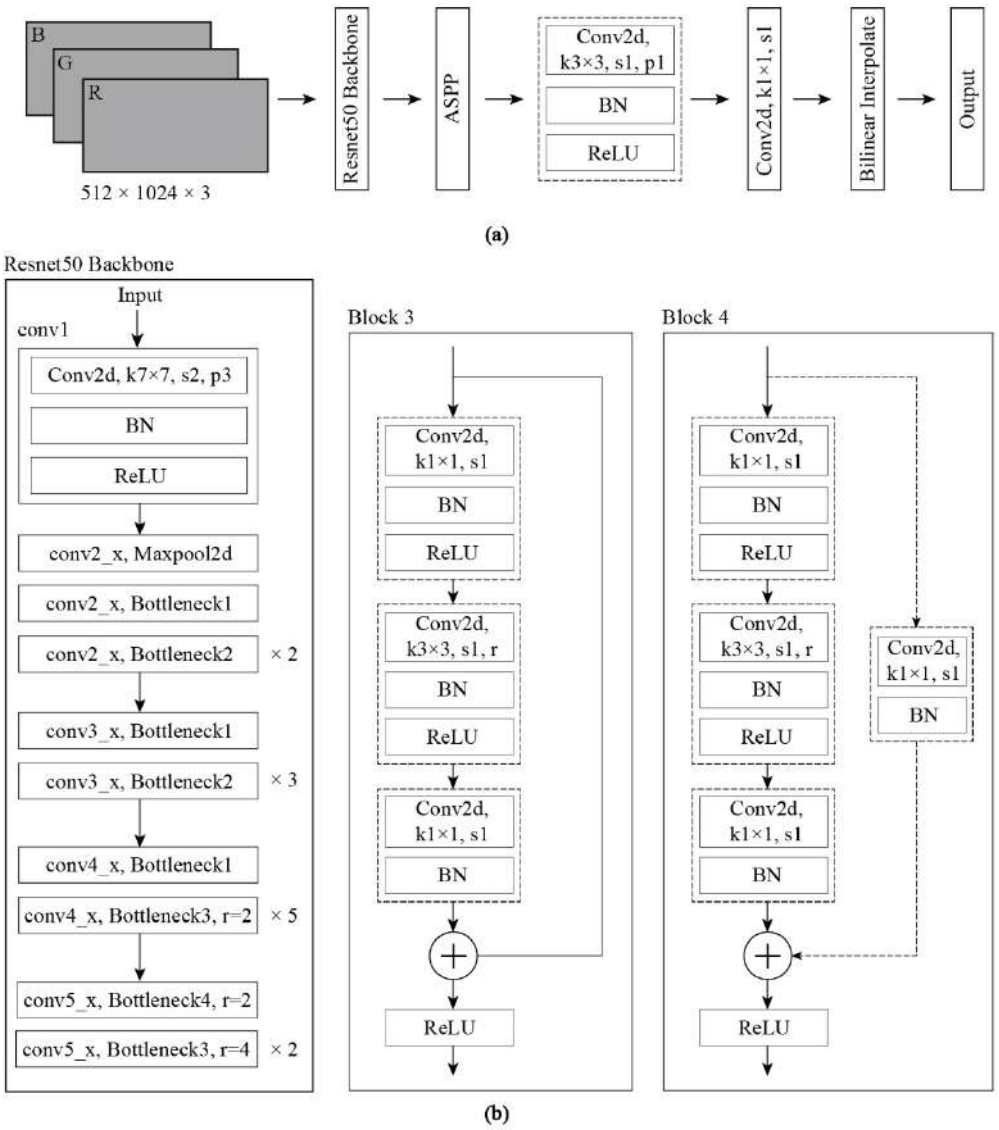

235 **Fig. 2** (a) DeepLabV3 structure for semantic segmentation of GSVPs; (b) ResNet50 backbone structure to extract hierarchical features of GSVPs

The output feature map from ResNet50 is fed into the atrous spatial pyramid pooling (ASPP) module (Fig. 3), which is a sophisticated method for multi-scale context information fusion. ASPP employs dilated convolutions with varying dilation rates to capture feature information
240 at different scales while preserving the resolution of the feature map. The outputs of the five sub-modules in ASPP are concatenated along the channel dimension, forming a richer feature representation. Subsequently, a 1x1 convolutional layer is employed to fuse these features, resulting in the final ASPP output.

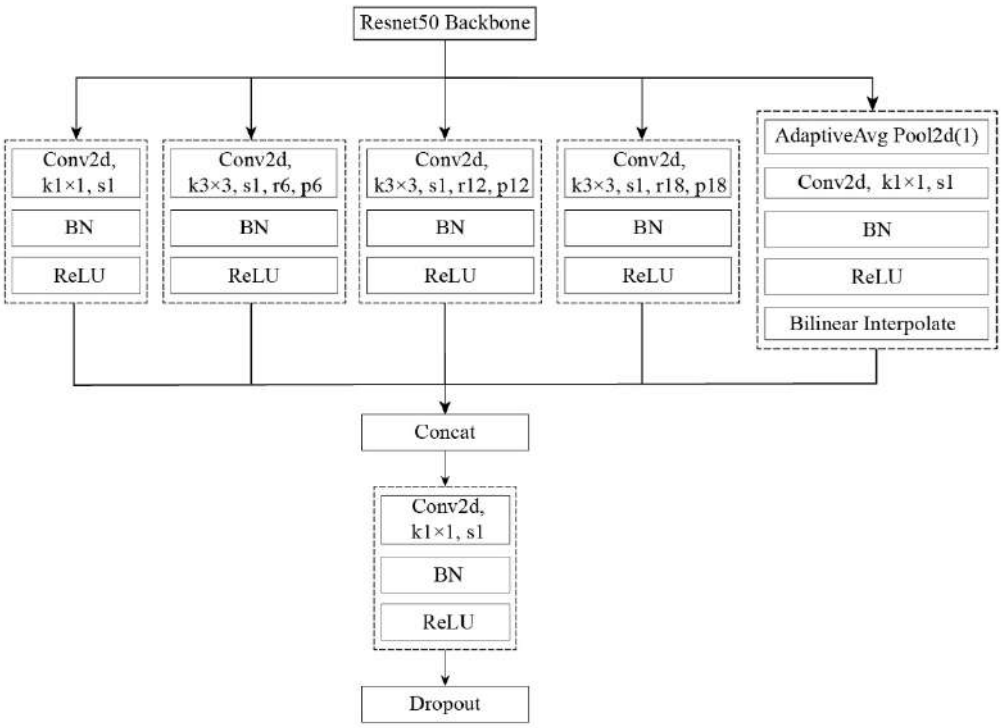

Fig. 3 ASPP structure to capture multi-scale contextual information

In the latter architecture of the DeepLabV3 model, a 3x3 convolutional layer is employed initially to attain a smoother and more continuous feature representation while retaining multi-scale features. Subsequently, a 1x1 convolutional layer is utilized to reduce the dimensionality of the feature map, thereby decreasing the computational burden and the number of model parameters, which in turn enhances computational efficiency. Ultimately, a bilinear interpolation up-sampling operation is adopted to restore the low-resolution feature map to the original image resolution, facilitating the extraction of street view features.

In this study, the open source Cityscapes Dataset is employed to train the DeepLabV3 model [38], which encompasses high-quality annotated urban street view images captured under various weather conditions and illumination levels across multiple cities. This enables the DeepLabV3 model to learn and generalize effectively across different scenarios. The 34 original label classes within the Cityscapes dataset are remapped to 20 distinct training label classes, which may exhibit considerable disparities in pixel count across images. For example, classes such as road and building may predominantly occupy the pixels within an image, whereas classes like pedestrian and bicycle may account for only a minor portion. Consequently, during the training process, the model may exhibit a proclivity for prioritizing classes with a higher pixel count, neglecting those with a lower count. This tendency could lead to suboptimal performance in less frequently occurring classes. To address this issue, it is necessary to balance the contributions of each class within the loss function by incorporating weights for each class. This involves assigning greater weights to classes with fewer pixels, thus ensuring increased attention during the training process and ultimately enhancing overall performance. Specifically, it is essential to quantify the pixel count of each class within the training set and subsequently calculate the respective weights [39]:

$$w_{class} = \frac{1}{\ln(1.02 + p_{class})} \tag{1}$$

in which w_{class} represents the weight of a specific class, and p_{class} denotes the proportion of the pixel count of a certain class relative to the total pixel count. In the training process, the DeepLabV3 model utilizes a weighted cross-entropy loss as the model's loss function. The loss function measures the difference between the predicted segmentation map and the true labels, guiding the model to minimize this difference by adjusting its weights during training. The entire procedure takes 1000 epochs, with a batch size of eight and an initial learning rate set to 1×10^{-4}.

Upon completing the training process of the DeepLabV3 model, the appropriate epoch training weights are utilized for precise semantic segmentation of the collected GSVPs, ensuring the optimal performance of the model while avoiding overfitting and underfitting. Subsequently, the segmented GSVPs undergo a hemispherical projection transformation, as it can capture the scenes in all directions from the observer's position, providing a more accurate environmental representation. As a result, the calculated view factors for the sky, tree, and buildings will more accurately reflect the coverage range of each category within the environment. These SVFs are saved in a CSV file to facilitate the next step of unsupervised classification.

3.3 Clustering analysis

The k-means algorithm is employed to categorize the features of each collection point stored in the CSV file. Each feature vector consists of eight dimensions, encompassing five GIS data points and three street view factors. Prior to executing the k-means classification, it is imperative to conduct absolute normalization on each feature vector to eliminate discrepancies in the data dimensions, thereby ensuring that the influence of each dimension on the classification outcome is equitably weighted and ultimately enhancing the classification accuracy.

K-means is an unsupervised learning algorithm employed for data clustering. Its fundamental concept involves partitioning the dataset into K categories, with each category represented by a centroid [40]. The objective of the algorithm is to minimize the sum of distances between each data point and the centroid of its corresponding category. Compared to other clustering algorithms, such as hierarchical clustering, which tends to be computationally expensive for large datasets, and density-based spatial clustering of applications with noise (DBSCAN), which suffers from sensitivity to noise and difficulties in defining optimal parameters, k-means has been proven to have low computational complexity, rapid convergence, and effective performance on large-scale datasets. However, it is sensitive to the selection of initial centroids, which may lead to local optima. Therefore, to determine the optimal K value, both the elbow method and silhouette coefficient are utilized [41].

The elbow method identifies the optimal K value by examining the changes in the sum of squared errors (SSE) corresponding to different K values [42]. As K increases, the SSE gradually decreases, but when K reaches a certain point, the decline in SSE significantly slows down. This point, referred to as the elbow, corresponds to the optimal K value. However, in some cases, the inflection point may not be apparent. To compensate for the potential limitations of using a single method, the silhouette coefficient [43], which considers both cohesion and separation in clustering, is also employed to find the optimal K value. The silhouette coefficient ranges between -1 and 1, with larger values indicating better clustering performance. By comparing the results of these two methods, a more balanced and rational optimal K value can be determined.

Upon determining the optimal K value, a statistical analysis of the k-means classification results is conducted. This includes the number of instances in each category and the mean

values of each dimension in the corresponding feature vectors, facilitating a more intuitive observation of the data differences between categories.

3.4 On-site thermal environmental data collection

To evaluate the thermal comfort associated with the K distinct categories derived from the previous step, 10 representative sampling locations are randomly selected from each category. These locations will undergo in situ measurements of air temperature T (unit: F) and relative humidity RH (unit: percentage).

Data collection is carried out using a Kestrel 4000 Weather and Environmental Meter, a state-of-the-art, portable instrument designed for precise measurements of meteorological variables. Measurements are taken every 15 minutes between 12:00 PM and 2:00 PM, a period when ambient temperatures typically reach their daily peaks. The average of these readings is calculated to ensure data accuracy. This time frame is chosen to better understand the potential heat stress faced by individuals during the hottest part of the day. The data collection process spans one month, with the exclusion of days when data acquisition is rendered infeasible due to adverse weather conditions, such as rainfall. However, due to uncontrollable factors such as varying levels of human activity, some uncertainty in the measurement data may still persist.

Upon completion of the data collection, the average heat index for each of the K categories is calculated using equation 2. By focusing primarily on the impact of air temperature and humidity on human perception, the heat index has been demonstrated to be a practical and straightforward approach to assessing the level of thermal comfort experienced by individuals in areas characterized by a predominantly hot and humid climate [44, 45]. Subsequently, a heat map representing the thermal gradient of the study area is generated, based on the average heat index corresponding to each category.

$$\begin{aligned} Heat\ index = {} & -42.379 + 2.04901523T + 10.14333127RH - 0.22475541TRH - \\ & 0.00683783T^2 - 0.05481717RH^2 + 0.00122874T^2RH + \\ & 0.00085282TRH^2 - 0.00000199T^2RH^2 \end{aligned} \quad (2)$$

4. Study area and datasets

This study concentrates on the Central and Western District and Wan Chai District in Hong Kong, both with their northern sides bordering the sea. This geographical condition subjects the local climate to a strong maritime influence, characterized by high humidity and rapid heat transfer. In this context, the high-density urban layout leads to particularly pronounced thermal discrepancies between streets. The southern sides of these two districts are built along mountains, resulting in a complex and varied urban structure with considerable variations in elevation and slope. To a certain extent, these prominent topographical features also affect the distribution and variation of the urban thermal environment. For instance, areas with steeper slopes may have less urban heat accumulation due to reduced direct sunlight exposure, while areas with higher elevation may be influenced by airflows, forming unique urban thermal environments. Hence, given the combined influences of a humid and hot climate, high-density urban layout, and complex and varied topography, these regions offer substantial reference value for examining the distribution of thermal gradient among urban streets.

Over the past 15 years, a substantial body of research has been dedicated to identifying more precise and efficient proxy parameters to achieve improved predictions and assessments of Hong Kong's urban thermal environments, ranging from building scale (<100m) to mesoscale (<200km) [46-48]. Conducting accurate and efficient thermal environment modeling on micro-scale (<2 km) samples and subsequently extending this knowledge to a broader context of urban street thermal environment classification is pivotal to advancing our understanding of

the street thermal gradient distribution in complex urban morphologies under typical climate conditions.

5. Data analyses, results, and findings

5.1 GIS data of collection points

According to the road network attributes of the study area, roads where people do not remain for a long time were removed, and a total of 11,675 GSVPs collection points were generated based on the remaining road network. To ensure quality of the panoramic images, all collected images were screened to exclude those with obvious abnormalities. For example, some roads were too narrow, resulting in excessively distorted perspectives in the panoramic images, or vehicles obscured the lens. After processing, a total of 8,538 GSVPs were collected. The locations of these collection points are shown in Fig. 4(a), distributed throughout the entire research area. The LULC of the research area consists of four categories: water, vegetation, urban, and bare surface, as shown in Fig. 4(b). The elevation and slope data of the whole research area are shown in Fig. 4(c) and (d). The elevation in the whole study area ranges from 0 to 1,245 meters, while the elevation of the collection points varies from 0 to 519 meters. As for the slope, it ranges from 0 to 64.43 degrees in the whole study area, and from 0 to 51.32 degrees at the collection points.

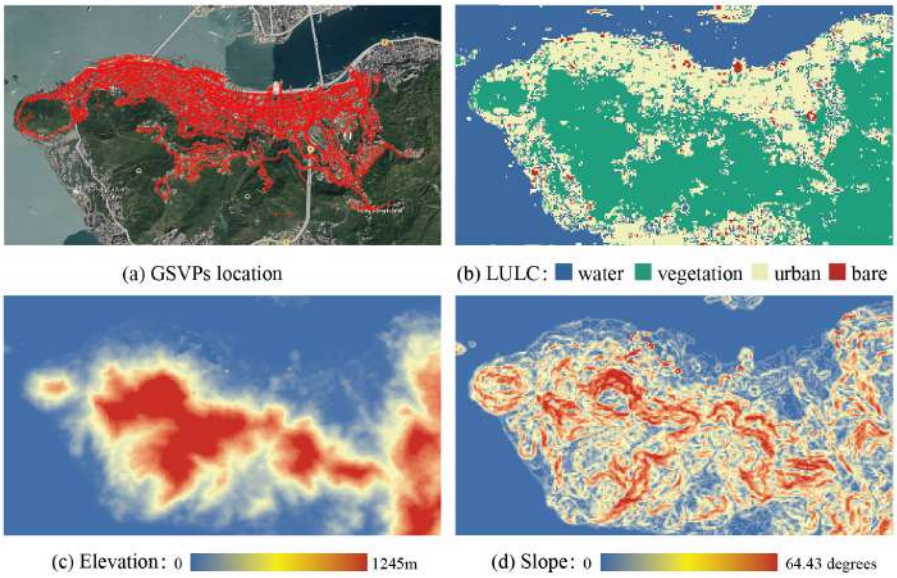

Fig 4. Five collected GIS data (i.e., longitude, latitude, LULC, elevation, and slope) in the study area

5.2 Street view factor of collection points

The DeepLabV3 semantic segmentation model and k-means unsupervised classification model are trained using the Pytorch on a Nvidia GeForce RTX 3060 GPU. It took 56.5 hours to train DeepLabV3 for 1000 epochs. The training and validation loss of DeepLabV3 are depicted in Fig 5. After the 200th epoch, the validation loss surpasses the training loss, and the training loss continues to decline, while the validation loss remains stagnant. This indicates that the model is learning the noise within the training data rather than the underlying patterns, resulting in poor generalization capabilities on unseen data. Therefore, the weight parameters obtained from training at the 200th epoch are utilized for semantic segmentation of the collected GSVPs.

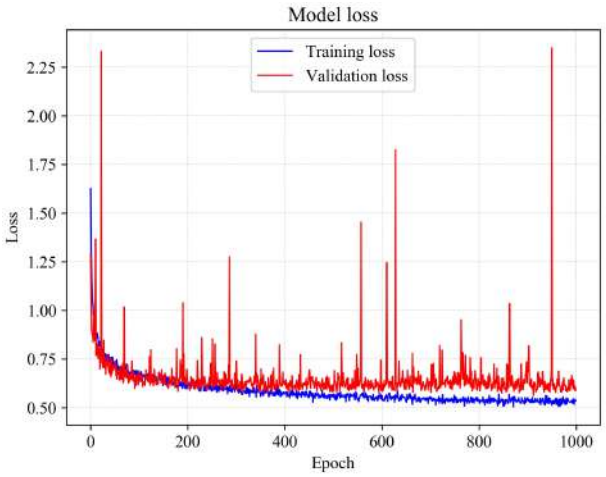

Fig 5. Training and validation loss in DeepLabV3 training process

The distribution of SVF, TVF, and BVF in the study area, as calculated from 8,538 semantically segmented GSVPs, is illustrated in Fig. 6. It is evident from the figure that the distribution of view factors exhibits geographical patterns. Specifically, coastal regions, owing to the limited obstructions and relatively open views, demonstrate better SVF performance. Additionally, sporadically distributed areas with higher SVF values can be observed in the main urban areas and elevated mountainous regions. These areas may benefit from the configuration of surrounding buildings and natural topography. Distribution of TVF presents a markedly different characteristic. Attributable to the natural advantages of mountainous areas, regions with better TVF performance are primarily concentrated in the southern hillside areas with considerable terrain undulations and lush vegetation. As for BVF, areas with larger values are predominantly situated in the central research area, characterized by high building density and relatively close distances between edifices. These distribution patterns reveal a certain clustering effect of view factors in geographic space, highlighting the crucial supporting and guiding role of view factors and geographic data in elucidating urban spatial structure and thermal environment classification.

In addition to the distribution characteristics in geographical space, to observe the gradient distribution of data more intuitively, the scale set on the color bar represents the view factor threshold of every 20% of the data in all 8358 GSVPs, revealing the changing trend and concentration area of the view factor values. For the data proportion of the three view factors, a notable common feature is that as the value decreases, the proportion of data gradually increases. This implies that in the studied urban space, these elements usually appear independently or in pairs in the majority of GSVPs pixels with a larger proportion. The balanced distribution of the three elements in the GSVPs is relatively rare, revealing the distinctiveness and extremeness of the urban element proportions. For instance, coastal urban areas generally exhibit better SVF performance, but due to poor soil and geological conditions and visual and landscape considerations, the corresponding TVF value is lower. Conversely, mountainous areas with better TVF performance may not be suitable for habitation, resulting in a lower corresponding BVF value. On the other hand, areas located in the city center, due to high building density, experience a certain degree of view limitation, with the maximum BVF reaching 92.95%, and the corresponding SVF and TVF values are smaller. This distinct and extreme element proportion characteristic exacerbates the clustering phenomenon in urban spaces, further corroborating the significant contribution of view factors and geographic data in the classification of Hong Kong's thermal environment.

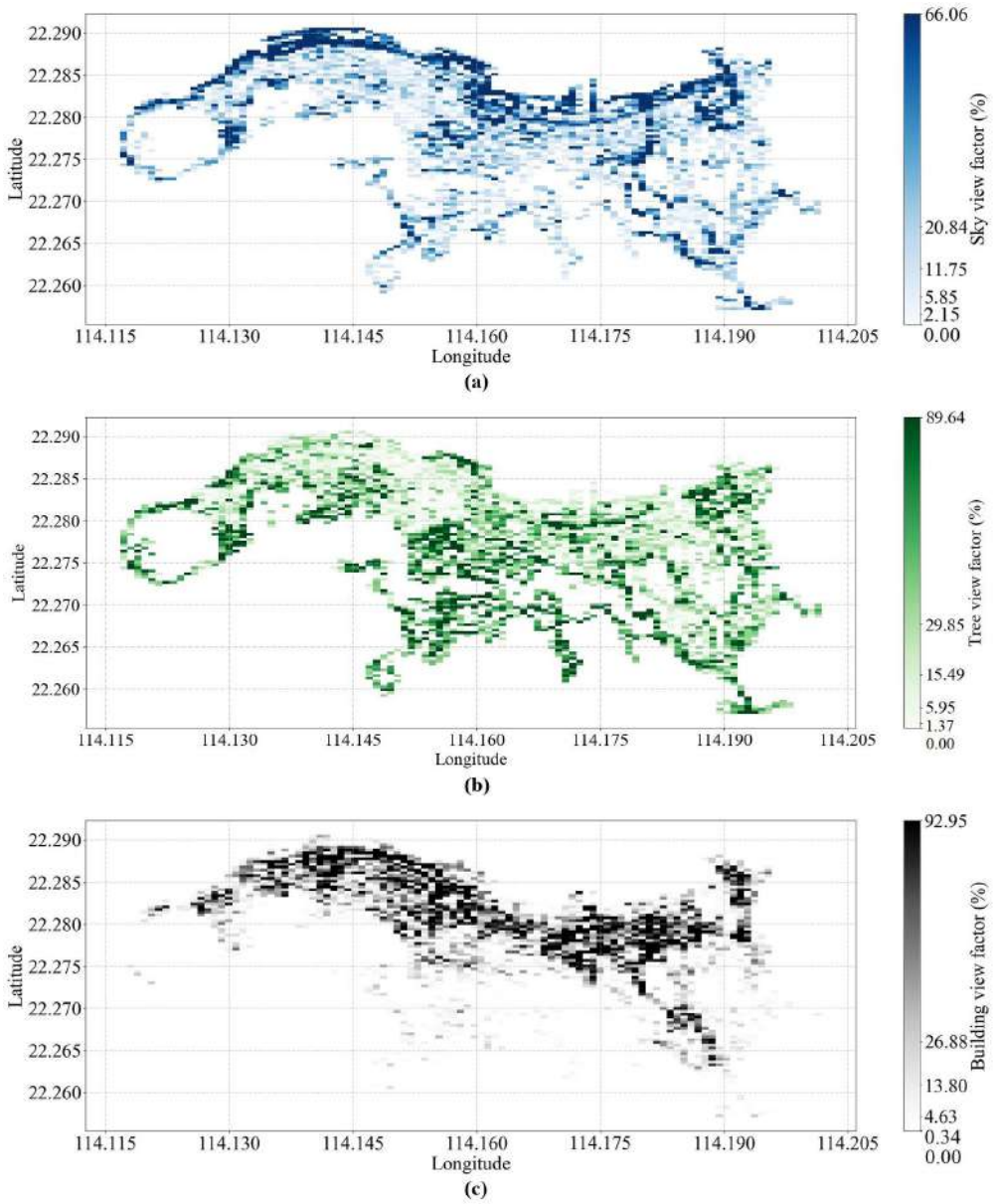

425 **Fig 6.** (a) SVF gradient distribution in the study area; (b) TVF gradient distribution in the study area; (c) BVF gradient distribution in the study area

5.3 Thermal environment classification of collection points

The variations in SSE and silhouette coefficient with respect to the number of clusters are depicted in Fig 7. In terms of the SSE calculated using the elbow method, although no distinct
430 elbow point can be observed, a notable deceleration in the reduction of SSE occurs within the range of 3 to 5 clusters, suggesting that a relatively suitable K value might exist around these cluster numbers. Regarding the silhouette coefficient, two prominent peaks are observed as the number of clusters increases, specifically when $K = 3$ and $K = 7$, with values ranging from 0.4 to 0.45. This outcome demonstrates that, at these two cluster numbers, the distances between
435 the sample points and other points within the same cluster are comparatively small, while the distances between different clusters are relatively large, resulting in a superior clustering effect. Therefore, after holistically considering the analysis results of the elbow method and silhouette coefficient, the optimal K value is determined to be 4.

It is worth noting that, although the geographical distribution of SVF, TVF, and BVF in the previous step allows for an intuitive division of the data into three clusters, corresponding to the coastal area, mountainous area, and urban center, these three view factors may not fully capture the complexity of spatial distribution, making it still challenging to define the clusters of over-urbanized regions. Upon incorporating multiscale and multilevel spatial information data, richer contextual information can be provided during the clustering process. By synergistically utilizing view factors and GIS data, the internal spatial relationships of the data are more accurately unveiled, leading to more rational clustering results.

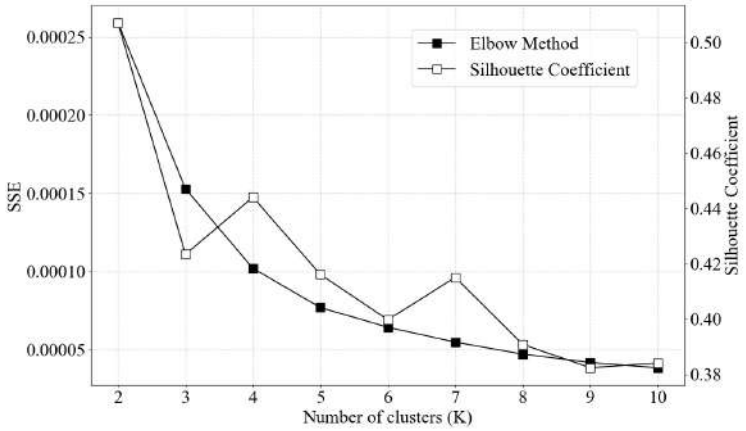

Fig 7. SSE and silhouette coefficient versus number of clusters

Upon determining the optimal *K* value, the average values of the clustering features for the 8358 GSVPs are presented in Table 1, and the feature distribution is shown in Fig 8. By examining the average feature values and their distribution in each category, a more detailed and comprehensive summary of the spatial characteristics of each cluster can be achieved compared to solely relying on the distribution of view factors. In cluster 0, excluding outliers, the identification values of LULC features for all the collected points are 1, indicating that this cluster consists entirely of urban areas. Taking into account factors such as elevation, slope, and view factor, it can be observed that the urban spaces represented by cluster 0 are characterized by relatively low elevations, gentle slopes, and the smallest average sky and tree coverage as well as the largest building coverage among the four clusters. These features suggest that cluster 0 embodies typical high-density urban center spaces or under-bridge spaces with limited greenery and obstructed sightlines. Hong Kong, as a quintessential high-density city, has a substantial amount of data for such spaces. Same as in cluster 0, the LULC identification values for all points in cluster 1 are also 1, representing urban areas. However, in terms of elevation and slope, cluster 1 is lower and more level compared to cluster 0, and the data distribution is more concentrated. Simultaneously, cluster 1 exhibits a larger sky coverage, indicating that these spaces tend to be located in urban areas with a relatively open field of vision (e.g., coastal areas, urban park, historic districts). The common characteristics of these areas include wide roads, a predominance of mid-rise buildings (4 to 12 stories), and ample space allocated for greening. These regions constitute the largest proportion within the study area.

Differing from the first two clusters, cluster 2 encompasses a diverse range of LULC classifications. The elevation and slope in this category are higher compared to the previous two classes, thus including areas with undeveloped or abandoned bare land surfaces. These areas are typically located at the urban fringes or the foot and mid-slopes of mountains, with

views predominantly consisting of the sky and trees. Cluster 3 exhibits the most distinct features, with a noticeable decrease in latitude and longitude compared to the first three clusters, and the highest elevation and steepest slopes. These spaces are largely mountain trails on the southern side of the study area, with minimal human intervention, resulting in a relatively smaller number of data collection points. In these regions, the natural environment is relatively well-preserved, with views primarily composed of native trees, and buildings being the least common sight.

Table 1. Number of collection points and average feature values for each category

Cluster	Count	Lng	Lat	LULC	Elevation	Slope	SVF	TVF	BVF
0	2886	114.16	22.28	1.06	32.14	11.66	4.94	5.05	30.64
1	3039	114.16	22.28	1.28	17.10	7.41	19.14	10.69	6.27
2	1924	114.16	22.27	2.05	109.80	17.73	11.07	30.46	4.82
3	689	114.15	22.26	2.56	346.85	19.96	10.90	43.80	2.22

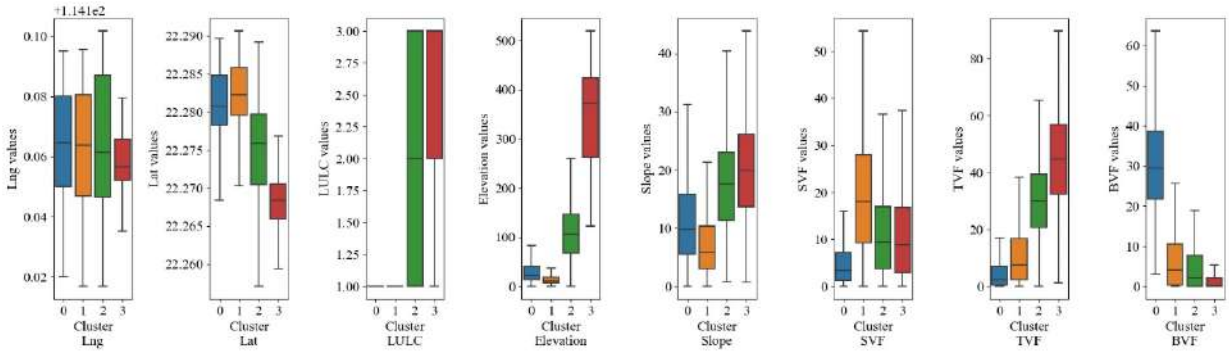

Fig 8. Boxplot of feature distribution for each cluster

5.4 Thermal gradient of collection points

In Fig 9, one example from 10 selected samples from each cluster for on-site measurements and its semantic segmentation results are presented. The data collection period spanned from 1–31 August, 2023. The heat index values are shown in Table 2, and the data distribution can be seen in Fig 10.

Regarding the average heat index and median line, although cluster 0 possesses the highest BVF (i.e., building density), its thermal environment is comparatively superior to that of cluster 1. Potential reasons for this include the extensive architectural shadows generated by high-rise buildings and aerial bridges, which obstruct or reflect a substantial amount of solar radiation, significantly mitigating the thermal environment of these types of street spaces. Conversely, cluster 1, with fewer obstructions, is exposed to direct sunlight for extended periods, resulting in the poorest thermal environment. Apart from the shading effect, the evapotranspiration of trees and their absorption of solar radiation notably enhance the thermal environments of clusters 2 and 3. Focusing on the maximum, minimum, and concentration of data, the data points in cluster 0 are predominantly situated in the urban center, where urban functions vary considerably, leading to a larger fluctuation range in the heat index. In contrast, the data within cluster 3, characterized by a relatively uniform morphological function, exhibits the most focused heat index.

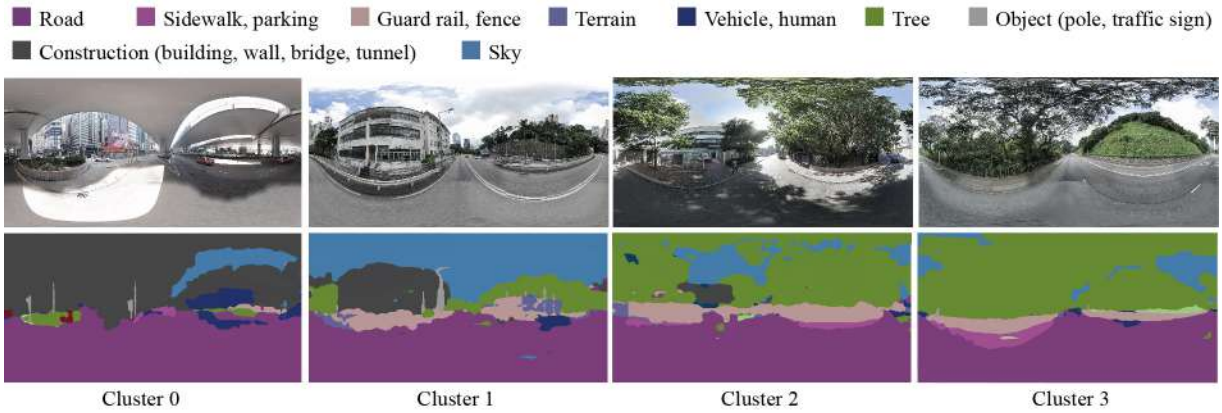

Fig 9. Samples and corresponding semantic segmentation results from each cluster

Table 2. Heat index values (°F) for samples of each category

Cluster	Maximum value	Average value	Minimum value
0	109.92	97.6	83.44
1	108.69	99.39	85.84
2	104.02	96.45	84.08
3	100.02	91.71	83.03

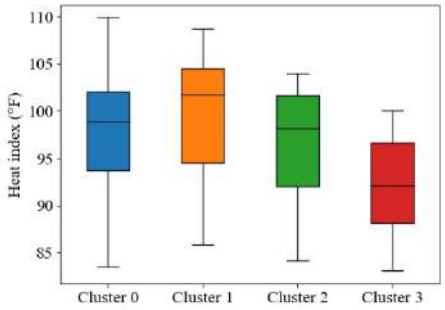

Fig 10. Boxplot of on-site heat index distribution for each cluster

The thermal gradient distribution of the four categories, as shown in Figure 11, confirms the earlier discussion. Data points in cluster 0, with the highest data fluctuations, are dispersed throughout the urban center, while data points included in cluster 3, with the most concentrated value, are predominantly located in the southern mountainous area of the study site. The data contained in cluster 1 are mostly located in the seashore and historical area while the data in cluster 2 are mostly located in the foothills. Moreover, the inclusion of detailed GIS data and the application of the k-means algorithm reveal a more distinct and clearer categorization of the spatial structure (i.e., thermal environment) within the urban area. Through this approach, the previously mixed street points within the over-urbanized area are effectively categorized into three separate categories.

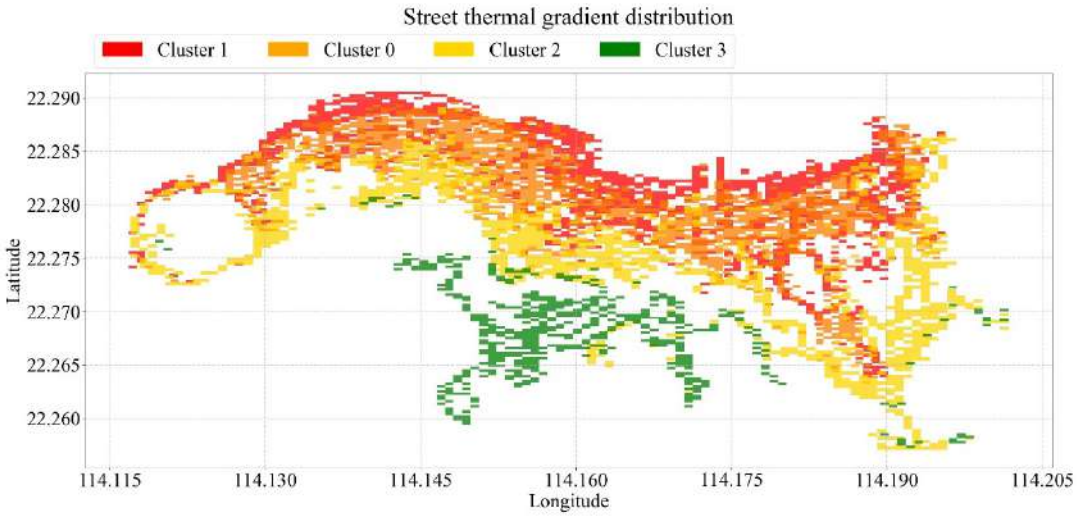

Fig 11. Street thermal gradient distribution in the study area

6. Discussion

6.1 Significance of the GIS-street view feature integration and k-means clustering

In multi-faceted metropolises, a vast array of urban transitional zones can be observed, such as coastal areas leading to high-density city centers and extending to mountainous regions, as well as the discrete distribution of older urban districts. These urban spaces exhibit diverse morphologies and functions, making it challenging to comprehensively depict these street spaces using only macro-scale GIS data or micro-scale street view features. This study effectively integrates these two types of data to provide a more in-depth understanding of the formation mechanisms underlying urban street thermal environments. Compared to existing thermal environment classification studies that rely solely on one type of data, this approach allows for a more comprehensive characterization of urban features. For instance, cluster 1, potentially representing coastal cities, can be defined by its higher latitude, lower elevation, and larger SVF. This enables a more accurate identification of the factors contributing to its poor thermal environment, offering targeted recommendations for future urban planning and management.

By employing the k-means clustering algorithm to categorize data with similar characteristics, knowledge pertaining to thermal environments can be extracted from the samples within each category and subsequently mapped onto the corresponding street categories. This approach ensures analytical accuracy while significantly mitigating the extensive time required for on-site measurements in previous SVI-based urban thermal environment classification studies due to the lack of historical data. As a result, it alleviates the tension between the low resolution associated with large-scale modeling and the extensive time investment required for high-precision modeling.

Based on the research findings, several key urban planning and design recommendations have been summarized to enhance overall street thermal comfort. Specifically, compared to cluster 2 and cluster 3, which have relatively favorable thermal environments due to large areas of vegetation coverage, cluster 1 has the poorest thermal comfort due to direct sunlight exposure, making it the most critical area for improvement. The lower BVF and highest SVF indicate that this area has substantial open space. Therefore, tree planting to reduce the SVF is an effective strategy to improve street thermal comfort in these regions. For cluster 0, although its average heat index is slightly better than that of cluster 1, the wide fluctuations suggest that

certain streets also require urgent improvement. Streets in this cluster feature the highest BVF and the lowest TVF and SVF, indicating limited space for tree planting. Consequently, improving urban design or reducing building heat dissipation becomes a priority. Examples of recommended measures include designing shading structures with high-reflectivity materials to reduce street heat exposure or optimizing heating, ventilation, and air conditioning (HVAC) system operations to minimize heat emissions.

6.2 Limitations and future works

This study considers the multi-scale spatial structural features of streets to determine their corresponding thermal environment levels. However, previous research has found that different spatial features have varying degrees of impact on the street thermal environment [49, 50]. For example, the degree of street greening and building density have a more significant impact on the thermal environment, while the influence of latitude and longitude is relatively smaller. Future work could focus on incorporating feature weights to enhance the accuracy and reliability of clustering results. One potential approach is to use principal component analysis (PCA) to reduce dimensionality while preserving key information, thereby identifying and prioritizing the most influential features. Alternatively, feature importance scores obtained from machine learning models, such as random forest or gradient boosting, could be utilized to assign weights to each feature based on their relative impact on the thermal environment. These weights could then be integrated into the clustering process, either by modifying the distance metric in k-means clustering or by adopting weighted clustering algorithms, thereby enhancing the interpretability of the results. In addition, future work could explore hybrid clustering techniques, such as combining traditional k-means clustering with hierarchical or density-based clustering, to further improve the stability and robustness of the classification. To ensure the representativeness and reliability of the data, more rigorous on-site measurement methods, including the use of structured questionnaires or stricter data collection protocols, could be implemented to reduce uncertainties in the measurements.

7. Conclusion

In this study, a comprehensive framework for high-precision urban street-level thermal gradient distribution auditing is proposed. The framework addresses the challenges of low resolution and inaccuracies due to large research scopes in previous urban thermal environment classification studies, as well as the inefficiencies caused by repetitive modelling of thermal environments or data collection. The backbone of the proposed framework is the k-means unsupervised clustering algorithm for grouping data points with similar structures. The algorithm takes the spatial structural features of street points (i.e., coordinate, LULC, elevation, slope, SVF, TVF, BVF) as input, derived from GIS and the DeepLabV3 model. Given the strong interdependence and mutual influence between street spatial structure and thermal environment, the thermal environment grade for each category is represented by the on-site measured data of representative samples within the category.

Compared to the rough, subjective classification of street spatial structural features (i.e., thermal environments) based solely on partial spatial structural features of street points (e.g., SVF, TVF, BVF), the comprehensive integration of high-precision GIS data and the k-means algorithm demonstrates significant improvement in differentiating performance. This is particularly evident in over-urbanized areas with complex and varied morphologies. It is recommended that future research incorporates weights for each spatial structural feature of street points to further enhance the performance of the k-means clustering algorithm and achieve higher precision in urban thermal gradient distribution modeling.

Acknowledgments

The study is supported by a Theme-Based Research Scheme (TRS) grant (Project No.: T22-504/21-R) and a Collaborative Research Fund (CRF) (Project No.: C7080-22GF), both from the Hong Kong Research Grant Council (RGC).

References

[1] F.E. Horton, D.R. Reynolds, Effects of Urban Spatial Structure on Individual Behavior, Economic Geography 47(1) (1971) 36-48. https://doi.org/10.2307/143224

[2] A. Anas, R. Arnott, K.A. Small, Urban Spatial Structure, Journal of Economic Literature 36(3) (1998) 1426-1464.

[3] P. Rickwood, G. Glazebrook, G. Searle, Urban Structure and Energy—A Review, Urban Policy and Research 26(1) (2008) 57-81. https://doi.org/10.1080/08111140701629886

[4] M.M. Rathore, A. Paul, W.-H. Hong, H. Seo, I. Awan, S. Saeed, Exploiting IoT and big data analytics: Defining Smart Digital City using real-time urban data, Sustainable Cities and Society 40 (2018) 600-610. https://doi.org/https://doi.org/10.1016/j.scs.2017.12.022

[5] M.F. Goodchild, Geographic information systems, Progress in Human Geography 15(2) (1991) 194-200. https://doi.org/10.1177/030913259101500205

[6] G.G. Wilkinson, A review of current issues in the integration of GIS and remote sensing data, International journal of geographical information systems 10(1) (1996) 85-101. https://doi.org/10.1080/02693799608902068

[7] J.C. Hinton, GIS and remote sensing integration for environmental applications, International journal of geographical information systems 10(7) (1996) 877-890. https://doi.org/10.1080/02693799608902114

[8] B. Hillier, J. Hanson, The social logic of space, Cambridge university press1989.

[9] A. Ståhle, L. Marcus, A. Karlström, Place Syntax: Geographic accessibility with axial lines in GIS, Fifth international space syntax symposium, Techne Press, 2005, pp. 131-144.

[10] Y. Ye, A.v.N. Nes, Quantitative tools in urban morphology: combining space syntax, spacematrix and mixed-use index in a GIS framework, Urban Morphology 18(2) (2014) 97-118. https://doi.org/10.51347/jum.v18i2.3997

[11] M.F. Goodchild, Scale in GIS: An overview, Geomorphology 130(1) (2011) 5-9. https://doi.org/https://doi.org/10.1016/j.geomorph.2010.10.004

[12] A.G. Rundle, M.D.M. Bader, C.A. Richards, K.M. Neckerman, J.O. Teitler, Using Google Street View to Audit Neighborhood Environments, American Journal of Preventive Medicine 40(1) (2011) 94-100. https://doi.org/https://doi.org/10.1016/j.amepre.2010.09.034

[13] N. He, G. Li, Urban neighbourhood environment assessment based on street view image processing: A review of research trends, Environmental Challenges 4 (2021) 100090. https://doi.org/https://doi.org/10.1016/j.envc.2021.100090

[14] F. Biljecki, K. Ito, Street view imagery in urban analytics and GIS: A review, Landscape and Urban Planning 215 (2021) 104217. https://doi.org/https://doi.org/10.1016/j.landurbplan.2021.104217

[15] D.A. Quattrochi, J.C. Luvall, Thermal infrared remote sensing for analysis of landscape ecological processes: methods and applications, Landscape Ecology 14(6) (1999) 577-598. https://doi.org/10.1023/A:1008168910634

[16] J.A. Voogt, T.R. Oke, Effects of urban surface geometry on remotely-sensed surface temperature, International Journal of Remote Sensing 19(5) (1998) 895-920. https://doi.org/10.1080/014311698215784

[17] Q. Weng, Thermal infrared remote sensing for urban climate and environmental studies: Methods, applications, and trends, ISPRS Journal of Photogrammetry and Remote Sensing 64(4) (2009) 335-344. https://doi.org/https://doi.org/10.1016/j.isprsjprs.2009.03.007

[18] M. Roth, T.R. Oke, W.J. Emery, Satellite-derived urban heat islands from three coastal cities and the utilization of such data in urban climatology, International Journal of Remote Sensing 10 (1989) 1699-1720. https://doi.org/10.1080/01431168908904002

[19] C.P. Lo, D.A. Quattrochi, J.C. Luvall, Application of high-resolution thermal infrared remote sensing and GIS to assess the urban heat island effect, International Journal of Remote Sensing 18(2) (1997) 287-304. https://doi.org/10.1080/014311697219079

[20] Q. Weng, D. Lu, J. Schubring, Estimation of land surface temperature–vegetation abundance relationship for urban heat island studies, Remote Sensing of Environment 89(4) (2004) 467-483. https://doi.org/https://doi.org/10.1016/j.rse.2003.11.005
[21] H. Huanchun, Y. Hailin, D. Xin, H. Cui, L. Zhifeng, L. Wei, Z. Peng, Analyzing the Influencing Factors of Urban Thermal Field Intensity Using Big-Data-Based GIS, Sustainable Cities and Society 55 (2020) 102024. https://doi.org/https://doi.org/10.1016/j.scs.2020.102024
[22] A. Iino, A. Hoyano, Development of a method to predict the heat island potential using remote sensing and GIS data, Energy and Buildings 23(3) (1996) 199-205. https://doi.org/https://doi.org/10.1016/0378-7788(95)00945-0
[23] V. Equere, P.A. Mirzaei, S. Riffat, Y. Wang, Integration of topological aspect of city terrains to predict the spatial distribution of urban heat island using GIS and ANN, Sustainable Cities and Society 69 (2021) 102825. https://doi.org/https://doi.org/10.1016/j.scs.2021.102825
[24] I. Maduako, Z. Yun, B. Patrick, Simulation and prediction of land surface temperature (LST) dynamics within Ikom City in Nigeria using artificial neural network (ANN), Journal of Remote Sensing & GIS 5(1) (2016) 1-7.
[25] A.A. Kafy, F. Abdullah Al, M.S. Rahman, M. Islam, A. Al Rakib, M.A. Islam, M.H.H. Khan, M.S. Sikdar, M.H.S. Sarker, J. Mawa, G.S. Sattar, Prediction of seasonal urban thermal field variance index using machine learning algorithms in Cumilla, Bangladesh, Sustainable Cities and Society 64 (2021) 102542. https://doi.org/https://doi.org/10.1016/j.scs.2020.102542
[26] J. Huang, X. Tang, P. Jones, T. Hao, R. Tundokova, C. Walmsley, S. Lannon, P. Frost, J. Jackson, Mapping pedestrian heat stress in current and future heatwaves in Cardiff, Newport, and Wrexham in Wales, UK, Building and Environment 251 (2024) 111168. https://doi.org/https://doi.org/10.1016/j.buildenv.2024.111168
[27] T.R. Oke, Canyon geometry and the nocturnal urban heat island: comparison of scale model and field observations, Journal of climatology 1(3) (1981) 237-254.
[28] F. Bourbia, F. Boucheriba, Impact of street design on urban microclimate for semi arid climate (Constantine), Renewable Energy 35(2) (2010) 343-347. https://doi.org/https://doi.org/10.1016/j.renene.2009.07.017
[29] E. Johansson, Influence of urban geometry on outdoor thermal comfort in a hot dry climate: A study in Fez, Morocco, Building and Environment 41(10) (2006) 1326-1338. https://doi.org/https://doi.org/10.1016/j.buildenv.2005.05.022
[30] R. Carrasco-Hernandez, A.R.D. Smedley, A.R. Webb, Using urban canyon geometries obtained from Google Street View for atmospheric studies: Potential applications in the calculation of street level total shortwave irradiances, Energy and Buildings 86 (2015) 340-348. https://doi.org/https://doi.org/10.1016/j.enbuild.2014.10.001
[31] D.R. Richards, P.J. Edwards, Quantifying street tree regulating ecosystem services using Google Street View, Ecological Indicators 77 (2017) 31-40. https://doi.org/https://doi.org/10.1016/j.ecolind.2017.01.028
[32] V.B. Andrew, E.T. John, C. Lee, U. David, R. Melanie, Modelling spatial and temporal road thermal climatology in rural and urban areas using a GIS, Climate Research 22(1) (2002) 41-55.
[33] X. Wei, F. Guan, X. Zhang, N. Van de Weghe, H. Huang, Integrating planar and vertical environmental features for modelling land surface temperature based on street view images and land cover data, Building and Environment 235 (2023) 110231. https://doi.org/https://doi.org/10.1016/j.buildenv.2023.110231
[34] United States Geological Survey. https://earthexplorer.usgs.gov/. (Accessed 20 Nov 2023).
[35] National Aeronautics and Space Administration. https://www.earthdata.nasa.gov/. (Accessed 20 Nov 2023).
[36] L.-C. Chen, G. Papandreou, F. Schroff, H. Adam, Rethinking Atrous Convolution for Semantic Image Segmentation, 2017, p. arXiv:1706.05587.
[37] K. He, X. Zhang, S. Ren, J. Sun, Deep residual learning for image recognition, Proceedings of the IEEE conference on computer vision and pattern recognition, 2016, pp. 770-778.
[38] Cityspaces. https://www.cityscapes-dataset.com/. (Accessed 13, Dec 2023).

[39] A. Paszke, A. Chaurasia, S. Kim, E. Culurciello, ENet: A Deep Neural Network Architecture for Real-Time Semantic Segmentation, 2016, p. arXiv:1606.02147.
[40] T. Kanungo, D.M. Mount, N.S. Netanyahu, C.D. Piatko, R. Silverman, A.Y. Wu, An efficient k-means clustering algorithm: analysis and implementation, IEEE Transactions on Pattern Analysis and Machine Intelligence 24(7) (2002) 881-892. https://doi.org/10.1109/TPAMI.2002.1017616
[41] C. Yuan, H. Yang, Research on K-Value Selection Method of K-Means Clustering Algorithm, J, 2019, pp. 226-235.
[42] M. Syakur, B. Khotimah, E. Rochman, B.D. Satoto, Integration k-means clustering method and elbow method for identification of the best customer profile cluster, IOP conference series: materials science and engineering, IOP Publishing, 2018, p. 012017.
[43] K.R. Shahapure, C. Nicholas, Cluster Quality Analysis Using Silhouette Score, 2020 IEEE 7th International Conference on Data Science and Advanced Analytics (DSAA), 2020, pp. 747-748.
[44] L.P. Rothfusz, N.S.R. Headquarters, The heat index equation (or, more than you ever wanted to know about heat index), Fort Worth, Texas: National Oceanic and Atmospheric Administration, National Weather Service, Office of Meteorology 9023 (1990) 640.
[45] G.B. Anderson, L. Bell Michelle, D. Peng Roger, Methods to Calculate the Heat Index as an Exposure Metric in Environmental Health Research, Environmental Health Perspectives 121(10) (2013) 1111-1119. https://doi.org/10.1289/ehp.1206273
[46] V. Cheng, E. Ng, C. Chan, B. Givoni, Outdoor thermal comfort study in a sub-tropical climate: a longitudinal study based in Hong Kong, International Journal of Biometeorology 56(1) (2012) 43-56. https://doi.org/10.1007/s00484-010-0396-z
[47] L. Zheng, W. Lu, L. Wu, Q. Zhou, A review of integration between BIM and CFD for building outdoor environment simulation, Building and Environment 228 (2023) 109862. https://doi.org/https://doi.org/10.1016/j.buildenv.2022.109862
[48] L. Zheng, W. Lu, Q. Zhou, Weather image-based short-term dense wind speed forecast with a ConvLSTM-LSTM deep learning model, Building and Environment 239 (2023) 110446. https://doi.org/https://doi.org/10.1016/j.buildenv.2023.110446
[49] A.J. Arnfield, Two decades of urban climate research: a review of turbulence, exchanges of energy and water, and the urban heat island, International Journal of Climatology 23(1) (2003) 1-26. https://doi.org/https://doi.org/10.1002/joc.859
[50] E. Ng, L. Chen, Y. Wang, C. Yuan, A study on the cooling effects of greening in a high-density city: An experience from Hong Kong, Building and Environment 47 (2012) 256-271. https://doi.org/https://doi.org/10.1016/j.buildenv.2011.07.014